PNAS RESEARCH ARTICLE | CHEMISTRY

Aluminum speciation identification reveals water interactions in silicoaluminophosphate zeolites

Caiyi Lou[a,b,1], Wenna Zhang[a,1], Pan Gao[c], Yida Zhou[a], Yuchun Zhi[a], Fangxiu Ye[a,b], Wenfu Yan[d], Shutao Xu[a,b,c,2], Yingxu Wei[a,b,c], and Zhongmin Liu[a,b,c]

Affiliations are included on p. 8.

Edited by Johannes Lehmann, Cornell University, Ithaca, NY; received April 2, 2025; accepted September 3, 2025

Water plays a crucial role in material development. As it is ubiquitous throughout zeolite generation and application, host–guest interaction between zeolite and water attracts broad interest, but mechanistic understanding remains fragmented. Here, advanced solid-state NMR techniques (2D ^{17}O SPAM-MQ, ^{27}Al{^{31}P} *J*-HMQC, ^{27}Al{^{29}Si} REDOR, and ^{1}H TQ-SQ NMR) combined with isotopic tracing and theoretical calculations determine water-induced octahedrally coordinated aluminum in silicoaluminophosphate molecular sieves (SAPOs) as an exclusive product of Al(OP)$_4$ units coordinated with two water molecules—a structure distinct from that in aluminosilicates. Based on the knowledge of aluminum speciation, we elucidate four water interaction mechanisms in SAPOs, including Brønsted-acid interaction, coordination, reversible/irreversible hydrolysis, and capillary condensation. Contrary to conventional wisdom attributing SAPO degradation to Al-O-P hydrolysis, we clarify that desilication dominates structural collapse, establishing Si environments as catalyst durability descriptors. These mechanistic insights decipher the nature of SAPO interacting with water and its fundamental differences from aluminosilicate zeolite.

water | zeolite | host–guest interaction | SAPO molecular sieve | aluminum species

Significance

Silicoaluminophosphate molecular sieves (SAPOs), a vital subclass of the zeolite family, have been demonstrating industrial prominence in catalysis and adsorption. Atom-level details of how they interact with water are imperative for both fundamental and practical advances in catalyst and adsorbent design, as water is ubiquitous throughout the zeolite lifespan and affects their framework dynamics. Herein, we identify the precise configuration of octahedrally coordinated aluminum, thereby clarifying the framework degradation mechanism and comprehensively elucidating four water interactions in SAPO. Such insights enable rational design of moisture-resistant SAPOs and advance their functionalities as high-performance sorbents for seawater desalination, atmospheric water harvesting, and chillers.

Host–guest interactions in zeolites have attracted considerable attention for decades (1–5), especially with water, as it is ubiquitous in zeolite synthesis, adsorption, catalytic reactions, and catalyst storage. (6–12) SAPOs, structurally analogous to aluminosilicate zeolites but compositionally distinct (as depicted in Fig. 1), play significant roles in industrial catalysis and adsorption. (13–16) They exhibit many peculiarities upon interacting with water compared to aluminosilicate zeolites, such as good hydrophilicity, (17) distinct adsorption behavior, (18, 19) and unusual hydrothermal stability, many SAPOs being susceptible for hydrolysis at room temperatures (20–25) but exceptionally stable at high temperatures under comparable-pressure conditions (26). Water-induced octahedrally coordinated aluminum species (Al^{VI}), converted from pristine tetrahedrally coordinated aluminum species (Al^{IV}), are invariably found in SAPO materials during hydration via ^{27}Al magic-angle spinning (MAS) NMR. Since their structures commonly provide abundant information regarding acidity, defect, and framework dynamic transformation, understanding the nature of Al^{VI} species is key to comprehending host–guest interactions between SAPOs and water, which is essential for both fundamental and practical advances in catalyst and adsorbent design, as well as for expanding the applications.

Solid-state NMR has long been an attractive approach for structural elucidation of zeolites, due to high sensitivity to minor changes in local environment, atom-scale details, and rich scalar/dipolar (through bond vs through space) interactions. Hunger et al. (27) systematically investigated the hydration and dehydration processes of SAPO-34 and SAPO-37 via in situ continuous flow MAS NMR spectroscopy and proposed two configurations for Al^{VI} species, i.e., framework Al (FAl) coordinated with two water molecules and framework-associated Al (FAAl) from partially hydrolyzed Al-O-P framework. Morriss et al., (28) Ashbrook et al. (29), and our recent work (30) have collectively demonstrated the rapid and reversible hydrolysis of T-O-T bonds in zeolites. Consequently, it is conceivable that Al^{VI} species might arise from reversibly hydrolyzed products of Al-O-T bonds, where the four Al-O bonds in the Al(OT)$_4$ moieties partially dissociate upon interacting with water and subsequently recondense completely after dehydration. Additionally, there is also a predisposition to associate Al^{VI} species with irreversible hydrolysis products of the Al-O-T framework (31–33) since SAPOs are typically susceptible for hydrolysis at ambient conditions and Al^{VI} species are generally attributed to extraframework Al (EFAl) or FAAl in aluminosilicate zeolites. (34–41) The formation of various Al^{VI} structures indicates different interaction mechanisms between SAPOs and water. To date, the precise

Author contributions: C.L., S.X., Y.W., and Z.L. designed research; C.L., W.Z., Y. Zhou, and F.Y. performed research; C.L., S.X., W.Z., P.G., Y. Zhi, W.Y., Y.W., and Z.L. analyzed data; and C.L. wrote the paper.

The authors declare no competing interest.

This article is a PNAS Direct Submission.

Copyright © 2025 the Author(s). Published by PNAS. This article is distributed under Creative Commons Attribution-NonCommercial-NoDerivatives License 4.0 (CC BY-NC-ND).

[1]C.L. and W.Z. contributed equally to this work.

[2]To whom correspondence may be addressed. Email: xushutao@dicp.ac.cn.

This article contains supporting information online at https://www.pnas.org/lookup/suppl/doi:10.1073/pnas.2507802122/-/DCSupplemental.

Published October 1, 2025.

Downloaded from https://www.pnas.org by CAS DALIAN INSTITUTE CHEMICAL PHYSICS on November 30, 2025 from IP address 119.78.131.208.

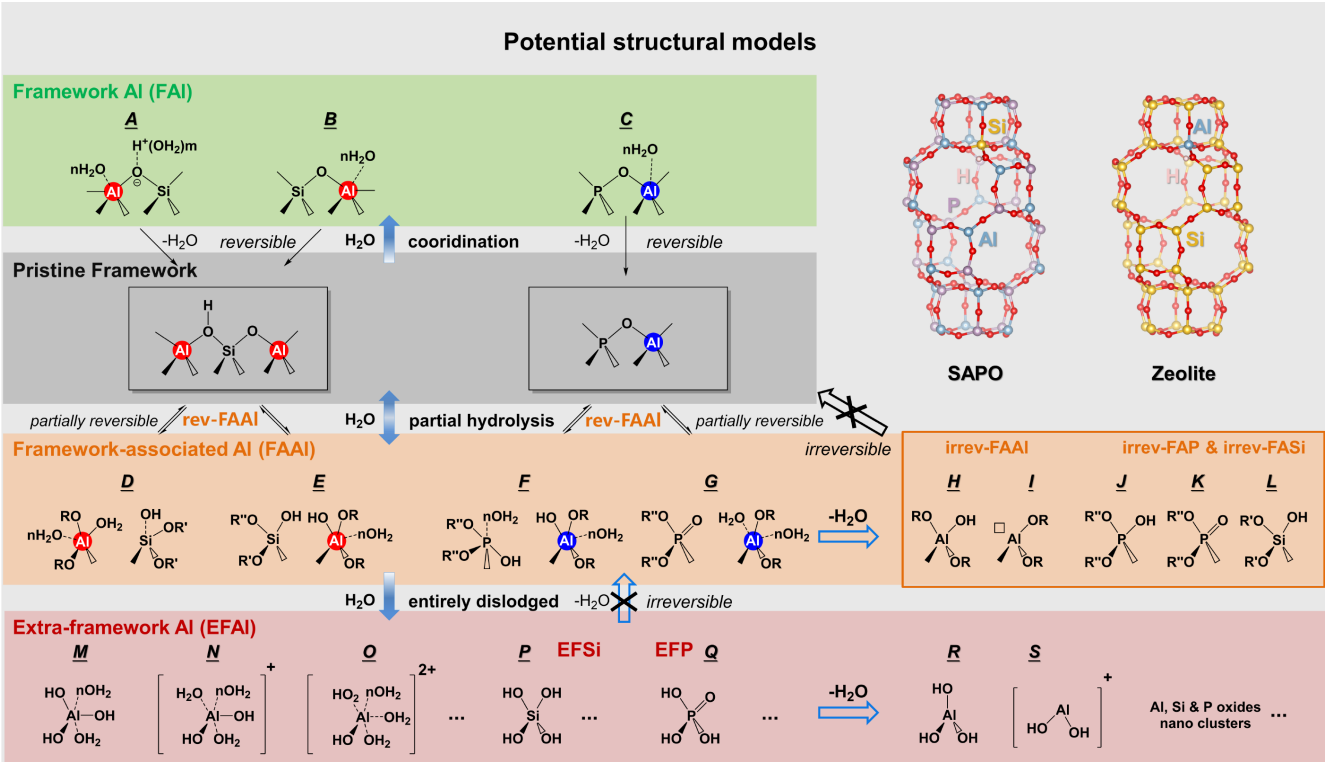

Fig. 1. Evolution of potential structural models in SAPO molecular sieves upon hydration and redehydration. Right 3D models comparing the elementary compositions of SAPOs and aluminosilicate zeolites as an example of CHA topology. FAP and FASi refer to framework-associated P and framework-associated Si moieties, respectively. Likewise, EFP and EFSi refer to extraframework P and extraframework Si, respectively. "n" represents the potential expanding coordination numbers of water: n = 0, Al^{IV}; n = 1, Al^{V}; n = 2, Al^{VI}; "m" denotes the number of water molecules in the water–proton complex. R = H, P, or Si; R′ = H, Al, or Si; R″ = H or Al.

structures of Al^{VI} species remain ambiguous, due to the knowledge gaps generated by multiple factors, including the underlying heterogeneity of Al^{VI}, framework lability (involving rapid and dynamic transformations), difficulty in distinguishing hydroxyl groups and water, and quadrupolar nature of ^{27}Al nucleus. Hence, it is imperative to be scrupulous in differentiating Al^{VI} types and separately validating all potential Al^{VI} configurations.

Bokhoven et al. reviewed Al species in aluminosilicate zeolites, highlighting their fundamental differences and calling for a more judicious usage of the terms of Al species. (36) Likewise, three categories of Al species potentially present in SAPOs are proposed here (Fig. 1), including FAl, FAAl, and EFAl. Therein, FAl is a framework-bonded species that merely expands its water coordination (green box). FAAl represents the Al species bonded to the framework but partially hydrolyzed (orange box) and can be subdivided into reversible FAAl (rev-FAAl) and irreversible FAAl (irrev-FAAl). Under hydration conditions, both rev-FAAl and irrev-FAAl species are depicted as structures *D, E, F* and *G*. Upon redehydration, rev-FAAl can be completely recovered to the initial pristine framework, whereas irrev-FAAl cannot be restored and instead exists as a defective Al species, such as structures *H* and *I*. EFAl denotes the Al species entirely dislodged from the zeolite framework and exists in the interstitial space (red box). Accordingly, three vital questions arise and are outlined as follows:

1. Contribution of EFAl, FAl, and FAAl, including rev-FAAl and irrev-FAAl, to the Al^{VI} species, respectively;
2. Contribution of the Al atoms from SiOH-Al$(OP)_3$, SiO-Al$(OP)_3$, and Al$(OP)_4$ moieties to the Al^{VI} species, respectively;
3. Degradation of SAPOs under ambient conditions: primarily results from the hydrolysis of Al-O-P, Al-O(H)-Si, or both.

In this work, SAPO-34 (**CHA**), the most successful catalyst applied in the methanol-to-olefins (MTO) industry (14) was selected to study water–zeolite interactions and explore the precise configuration of Al^{VI} species in detail. Aluminosilicate (SSZ-13) and aluminophosphate (AlPO-34) zeolites with the same **CHA** topology, as well as SAPOs with high hydrolysis sensitivity, including DNL-6 (RHO), SAPO-37 (FAU), and SAPO-42 (LTA), were employed for the comparison of water–zeolite interactions. The hydration conditions used here were neutral and ion-free, given that aluminophosphate is amphoteric, soluble in both acidic and alkaline media. Quantitative ^{27}Al and 2D $^{27}Al\{^{31}P\}$ NMR spectroscopy demonstrated the negligible contribution of EFAl to Al^{VI} species. Advanced multiple-quantum (MQ) NMR and ^{27}Al-$^{29}Si/^{31}P$ correlation NMR techniques, combined with ^{17}O isotope tracing and ^{29}Si labeling, further revealed the precise configuration of Al^{VI}. Furthermore, integrating ^{1}H homonuclear triple-quantum-single-quantum (TQ-SQ) correlation NMR, theoretical calculations, and water adsorption experiments provided thorough insights into the host–guest interactions between SAPOs and water, covering structural dynamics, degradation mechanism, and adsorption behavior. By deciphering the Al^{VI} species after hydration, this work sheds light on the nature of the SAPOs interacting with water and promotes their rational design for desired applications.

Results and Discussion

Negligible Contribution of EFAl to Al^{VI} Species. SAPO-34 (8.8% Si content, sole $Q^4(4Al)$ environment) and SSZ-13 (5.6% Al content) with comparable Brønsted acid quantities are first explored, and AlPO-34 and high-silicon content SAPO-34 (18% Si content, multiple $Q^4(nAl)$ environments) samples are

Downloaded from https://www.pnas.org by CAS DALIAN INSTITUTE CHEMICAL PHYSICS on November 30, 2025 from IP address 119.78.131.208.

also included for comparison. Their corresponding synthesis methods and structure information are detailed in the Supporting Information (*SI Appendix*, Tables S1 and S2 and Figs. S1–S3).

In Fig. 2*A*, dehydrated H-SSZ-13 exhibits a broad ^{27}Al signal at ca. 17 ppm, whereas hydrated H-SSZ-13 shows two sharp signals: a predominant Al^{IV} peak at 59 ppm and negligible Al^{VI} at -3 ppm. The signal discrepancy emphasizes that the hydration treatment is commonly a prerequisite for ^{27}Al NMR analysis of aluminosilicate zeolites due to reduced quadrupole coupling constant (C_Q). In contrast, both dehydrated and hydrated H-SAPO-34 samples (Fig. 2*B*) show relatively narrow ^{27}Al peaks. Although dehydrated H-SAPO-34 shows only one Al^{IV} signal at 36 ppm, ^{27}Al MQ MAS NMR resolves contributions from $SiOH\text{-}Al(OP)_3$, $SiO\text{-}Al(OP)_3$, and $Al(OP)_4$ moieties (*SI Appendix*, Fig. S2*A*). During hydration, a strong Al^{VI} signal at ca. -12 ppm and a weak penta-coordinated Al (Al^{V}) signal near 16 ppm emerge, and the initial Al^{IV} signal shifts from 36 to 42 ppm. The chemical shift variation of Al^{IV} species (from 36 to 42 ppm) arises from deshielding effects induced by framework distortion upon water adsorption. Upon further redehydration, Al^{V} and Al^{VI} signals disappear, recovering the initial Al^{IV} species. SAPOs with other topologies (*SI Appendix*, Fig. S4) and AlPO-34 (*SI Appendix*, Fig. S5) also manifest similar changes with H-SAPO-34. Therefore, the Al^{IV}-Al^{VI} reversible transformation universally occurs in SAPOs upon the hydration/dehydration cycles. In addition, contrasting Al^{VI} populations between H-SSZ-13 and H-SAPO-34 implies that they are fundamentally distinct species.

The $^{27}Al\{^{31}P\}$ scalar coupling correlation (*J*-HMQC) NMR spectrum of the hydrated H-SAPO-34 (Fig. 2*C*) reveals the bond connections between Al and framework P atoms, showing strong correlations of Al^{IV}, Al^{V}, and Al^{VI} species with framework P atoms. Likewise, DNL-6 and AlPO-34 (*SI Appendix*, Fig. S6 *A* and *B*) show consistent results, confirming that most Al^{VI} atoms are bonded to at least one framework P atom and suggesting the virtual absence of EFAl species. Furthermore, EFAl species, existing as several oxide and hydroxide forms such as $Al(OH)_3$ or

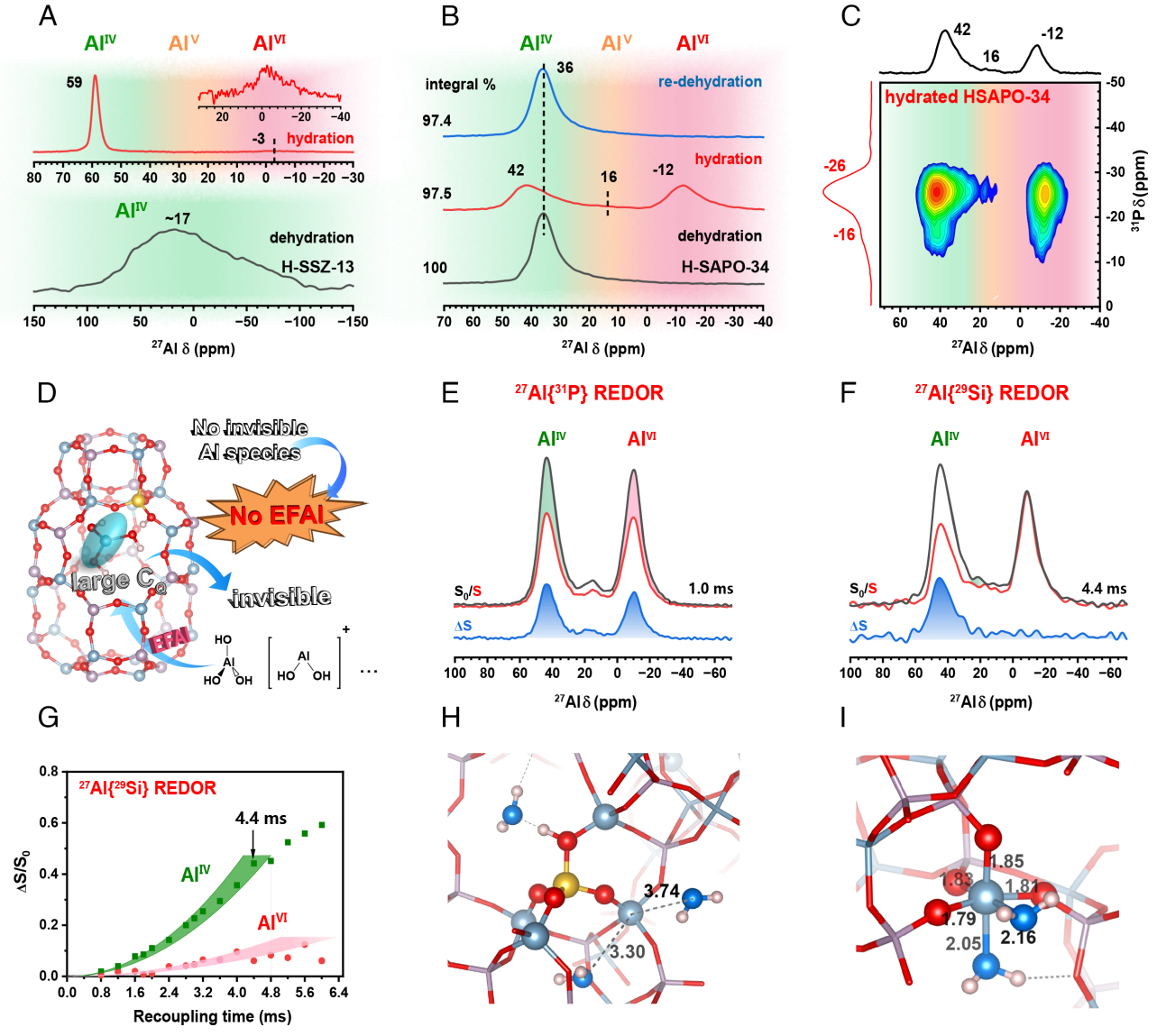

Fig. 2. Connections and proximities of Al species to framework atoms. (*A* and *B*) ^{27}Al MAS NMR spectra of H-SSZ-13 with Si/Al = 17 and H-SAPO-34 with Si mole content of 8.8%, respectively. (*C*) $^{27}Al\{^{31}P\}$ *J*-HMQC NMR spectrum of hydrated H-SAPO-34 using a recoupling time of 5.0 ms. (*D*) Schematic figure of the negligible contribution of EFAl to Al^{VI} species. (*E*) $^{27}Al\{^{31}P\}$ REDOR MAS NMR spectra of hydrated H-SAPO-34, comparing a ^{31}P recoupling time of 1.0 (red line) and 0 ms (gray line). (*F* and *G*) $^{27}Al\{^{29}Si\}$ REDOR MAS NMR spectra of hydrated ^{29}Si-enriched H-SAPO-34 comparing a ^{29}Si recoupling time of 4.4 (red line) and 0 ms (gray line), and corresponding build-up curves with varying recoupling times, respectively. (*H* and *I*) Optimized geometries of the interaction between water and Al atom within the intact $SiO\text{-}Al(OP)_3$ and $Al(OP)_4$ framework, respectively. (pink = H, red = framework O, blue = water O, cerulean = Al, amber = Si, and lavender = P).

Downloaded from https://www.pnas.org by CAS DALIAN INSTITUTE CHEMICAL PHYSICS on November 30, 2025 from IP address 119.78.131.208.

multinuclear clusters, are normally undetectable by ^{27}Al NMR after dehydration due to prominent quadrupolar broadening [large C_Q, usually > 30 MHz (42)], much broader than Al^{IV} in dehydrated aluminosilicate zeolites [14–18 MHz (43, 44)] as the dehydrated H-SSZ-13 shown in Fig. 2*A*. So EFAl species are also referred to as "invisible Al species" under dehydration conditions. (35, 37, 45, 46) Hence, a detailed quantitative estimation can reveal the amount of invisible EFAl species by comparing in situ ^{27}Al MAS NMR under dehydration and hydration using a small flip-angle ($\leq \pi/18$) excitation. Total ^{27}Al integrals in H-SAPO-34 (Fig. 2*B*, integral %), as well as in other SAPOs (*SI Appendix*, Table S3), exhibit little to no change after hydration and subsequent redehydration. As illustrated in Fig. 2*D*, these results demonstrate that no detectable amounts of invisible EFAl debris are generated in SAPOs after interacting with water at room temperature, even in cases where severe framework degradation occurs, such as in DNL-6, SAPO-42, and SAPO-37 evidenced by the incomplete recovery of their ^{31}P NMR spectra (*SI Appendix*, Fig. S7).

Resistance of Al Atoms from Al-O(H)-Si Moieties to Water Coordination. The above discussions confirm that most Al^{VI} atoms of H-SAPO-34 are bonded to at least one P framework atom. However, contributions from Al atoms in SiOH-Al(OP)$_3$ and SiO-Al(OP)$_3$ moieties, including FAl (structures *A* and *B*) and FAAl (*D*and *E*), to Al^{VI} signals remain uncertain. To further elucidate the chemical environments of the Al atoms, rotational echo double resonance (REDOR) NMR was introduced to obtain distance information between the Al atom and adjacent heteroatoms, where the degree of attenuation is inversely proportional to the ^{27}Al-X dipole coupling constant or distance. It should be mentioned that the Al-OH-Si and Al-O-Si moieties are unified as one form and represented as Al-O(H)-Si under hydration conditions since proton dissociation and exchange occur constantly.

^{27}Al{^{31}P} REDOR MAS NMR spectra of the hydrated H-SAPO-34 (Fig. 2*E*) show comparable attenuations ($\Delta S/S_0$) of Al^{IV} (35.5%) and Al^{VI} (32.4%) signals with applying a ^{31}P irradiation recoupling time of 1.0 ms, and the corresponding build-up curves (*SI Appendix*, Fig. S6 *C* and *D*) as a function of recoupling time almost overlap, which is also the case for H-DNL-6 (*SI Appendix*, Fig. S6 *E* and *F*). In AlPO-34 (*SI Appendix*, Fig. S6 *G* and *H*), the Al^{IV} (41.5%) decays faster than Al^{VI} (33.7%, comparable to Al^{VI} in H-SAPO-34) with a recoupling time of 1.0 ms and even faster than Al^{IV} (35.5%) in H-SAPO-34. This indicates that the coordination of water molecules elongates the Al-P distance in Al^{VI} species, while both hydrated SAPO and AlPO frameworks share similar phosphorus coordination environments for Al^{VI}. Furthermore, the smaller attenuation of Al^{IV} (35.5%) in H-SAPO-34 compared to AlPO-34 (41.5%) confirms the signal contribution of SiO(H)-Al(OP)$_3$ structures to Al^{IV} in SAPOs, which structures inherently exhibit slower decay than Al(OP)$_4$. For the ^{27}Al{^{29}Si} REDOR NMR experiment, 99.2% ^{29}Si-labeled SAPO-34 was intentionally synthesized and utilized to maximize the dephasing results and improve the accuracy for estimating the spatial proximity of Al atoms to Si, since the natural isotopic abundance of ^{29}Si is as low as 4.68%. The results exhibit a strong attenuation for Al^{IV} (44.2%) and a minimal attenuation for Al^{VI} signal (6.1%) at a recoupling time of 4.4 ms for ^{29}Si irradiation (Fig. 2*F*). Corresponding build-up curves (Fig. 2*G*) show that the dephasing of Al^{IV} species becomes gradually pronounced over 60.0% with increasing recoupling time, while that of Al^{VI} is always below 12%. This indicates that a substantial proportion of Al^{IV} species are in proximity to Si atoms, whereas Al^{VI} species are hardly associated with Si atoms. Therefore, the Al^{IV} signal in hydrated SAPOs is derived from at least a twofold superposition of SiO(H)-Al(OP)$_3$ and Al-(OP)$_4$, while the Al^{VI} signal mainly stems from Al-(OP)$_4$ moiety. The Al atoms from SiOH-Al(OP)$_3$ or SiO-Al(OP)$_3$ moieties exhibit resistance to water coordination, retaining the tetrahedral coordination.

Additionally, it is worth noting that all framework Al atoms are related to the Brønsted acid protons in aluminosilicate zeolites, whereas only one-quarter of the Al atoms surrounding Si atoms are involved in the creation of the bridged hydroxyl in the SAPO frameworks (1 SiOH-Al(OP)$_3$: 3 SiO-Al(OP)$_3$). (47, 48) Nonetheless, all Al species in proximity to the framework Si atom, regardless of whether the Al atom originates from an Al-O-Si or Al-OH-Si moiety and whether it is partially hydrolyzed, exclusively adopt a tetrahedral configuration in SAPOs under hydration conditions rather than an octahedral one. Therefore, despite the crucial impact of the acidic proton on maintaining tetrahedral coordination, bonding with the proton is not a prerequisite for Al atoms to prevent water coordination.

Theoretical simulations of the interaction between water and the Al atoms within the intact SiO-Al(OP)$_3$ and Al(OP)$_4$ frameworks also confirm the above conclusion. As shown in Fig. 2 *H* and *I*, the distances between the Al atom within SiO-Al(OP)$_3$ and the O atom in the two water molecules are 3.3 and 3.7 Å, respectively, being over 1.5 Å longer than the framework Al-O distance (≈1.8 Å). In contrast, within Al(OP)$_4$, the distances are 2.1 and 2.2 Å, just slightly longer than 1.8 Å, confirming the formation of strong coordination bonds.

Reversible Hydrolysis and Contribution of FAAl to Al^{VI} Species. Since the above discussions exclude the contribution of Al from Al-O(H)-Si moieties to Al^{VI}, Al^{VI} species predominately originate from the Al(OP)$_4$ moieties. Yet, whether the Al^{VI} species is hydrolyzed is still unknown. As a fundamental criterion for T-O-T hydrolysis, identifying hydroxyl group species is key to distinguishing FAAl from FAl. Hydroxyl group defects of irrev-FAAl species (structures *H* or *I* in Fig. 1) can be identified by ^{1}H NMR spectroscopy after redehydration. Fig. 3*E* shows Al-OH defects (2.6 ppm) in DNL-6 and high-silicon SAPO-34 (HSi-SAPO-34) after redehydration, since Al-OH defects generally do not condense or dehydroxylate during dehydration. However, distinguishing the hydrophilic hydroxyl groups of rev-FAAl species (structures *D, E, F* and *G*) from water is challenging, given that they are only produced under hydration and completely recovered to the pristine framework Al^{IV} after dehydration. Some researchers inferred that Al-O-P bonds are at least partially hydrolyzed after water exposure, since the P-OH signal was claimed to be identified under hydration according to the enhancement of that signal (ca. −15 ppm) in ^{31}P{^{1}H} Cross Polarization (CP) MAS NMR spectra. (27, 49) Theoretically, the CP experiment cannot appropriately differentiate between P-OH and the framework P atoms associated with water. Hence, it is vital to explore and develop effective methodologies for investigating rev-FAAl species in SAPOs.

The computational density functional theory (DFT) method provides a good opportunity to address this issue. As displayed in Fig. 3 *A* and *B*, the hydrolysis barriers of the Al-O-Si bond within SiOH-Al(OP)$_3$ moiety and the Al-O-P bond within Al(OP)$_4$ moiety, each interacting with one water molecule, were compared. Both scenarios involve vicinal diol structure intermediates (S2/P2). The energy barrier of Al-O-P hydrolysis (127.5 kJ·mol^{-1}) is much higher than that of Al-O-Si hydrolysis (68.9 kJ·mol^{-1}). The hydrolysis of the Al-O-Si bond is exothermic with an energy of −30.0 kJ·mol^{-1}, contrary to that of the Al-O-P bond with an endothermic energy of 52.4 kJ·mol^{-1}. From a theoretical point of view, this demonstrates that the Al-O-P bond is more stable

Downloaded from https://www.pnas.org by CAS DALIAN INSTITUTE CHEMICAL PHYSICS on November 30, 2025 from IP address 119.78.131.208.

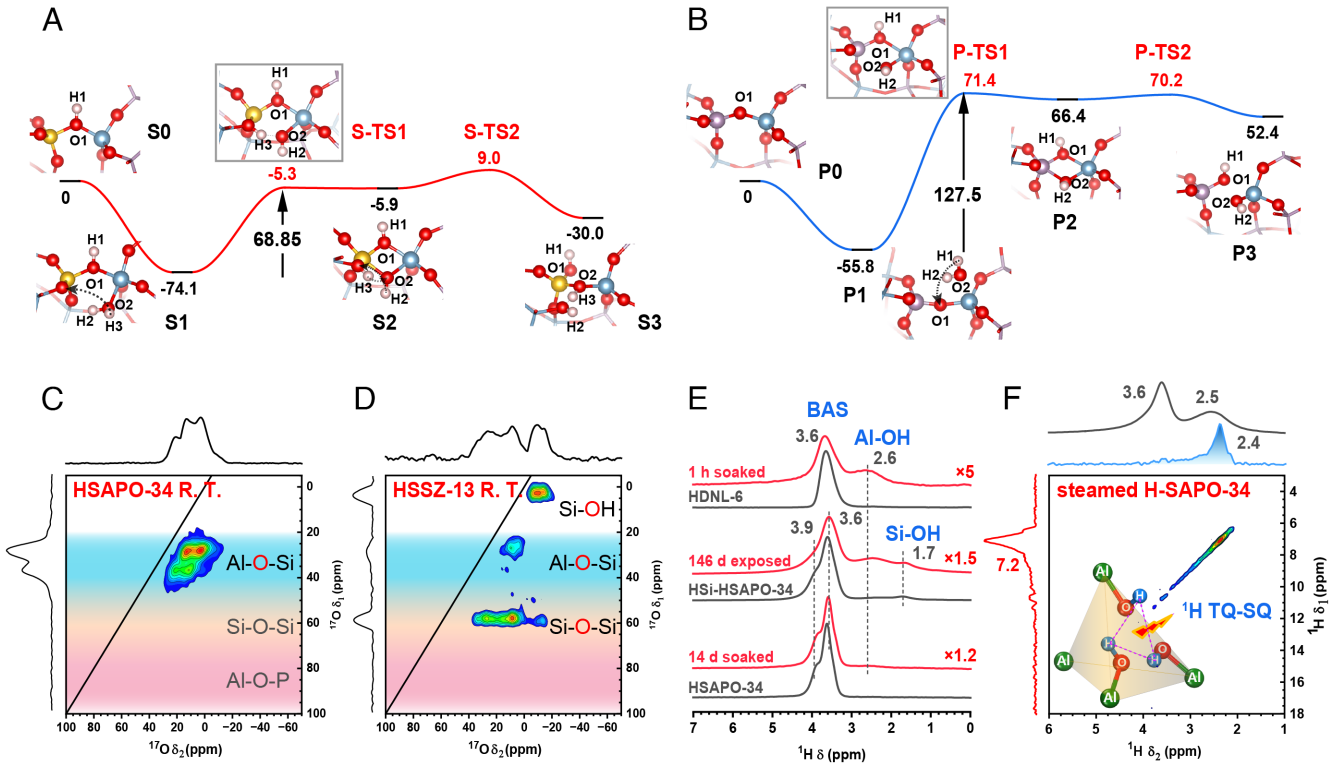

Fig. 3. SAPO framework reversible hydrolysis and structural degradation. (*A* and *B*) Potential energy profiles (in kJ·mol^{-1}) for hydrolysis of the first Al-O-Si and Al-O-P bond through the vicinal diol structure, respectively. (pink = H, red = O, cerulean = Al, amber = Si, and lavender = P) (*C* and *D*) 2D ^{17}O MQ MAS NMR spectra of dehydrated zeolites after $H_2{}^{17}O$ soaking at room temperature. (*E*) ^{1}H MAS NMR spectra of dehydrated H-SAPO-34, HSi-H-SAPO-34, and H-DNL-6 acquired at an 11.7 T magnet in 3.2 mm rotors. (*F*) 2D ^{1}H TQ-SQ MAS NMR spectrum of 130 °C steamed H-SAPO-34, whose top black line is the single pulse ^{1}H NMR spectrum. The steamed sample was treated in the autoclave with autogenous vapor pressure.

against hydrolysis than the Al-O-Si bond. Experimentally, instead of directly characterizing hydroxyl groups, ^{17}O tracing methods offer an innovative strategy to study the hydrolysis process of materials. Upon contact with $H_2{}^{17}O$, the ^{17}O exchange will be recorded by ^{17}O MAS NMR if the reversible hydrolysis occurs. For H-SAPO-34, the SPAM (soft-pulse-added-mixing) approach, introduced by Gan (50) and Amoureux (51–53), was employed to enhance the SNR of MQ spectra (Fig. 3*C*), in comparison to the z-filter method (*SI Appendix*, Fig. S8). Fig. 3 *C* and *D*, and *SI Appendix*, Fig. S9 display the ^{17}O MQ MAS NMR spectra of H-SAPO-34, H-SSZ-13, and as-made SAPO-34 (tem-SAPO-34) samples after room-temperature $H_2{}^{17}O$ soaking, respectively. Strong Al-^{17}O-Si linkages ($\delta_1 \approx 20$~50 ppm) are present in H-SAPO-34 and tem-SAPO-34 without any Si-^{17}O-Si or Al-^{17}O-P signals. H-SSZ-13 shows significant Al-^{17}O-Si, Si-^{17}O-Si, and Si-^{17}OH signals. Therefore, in both aluminosilicate zeolites and SAPOs, rapid and reversible hydrolysis of Al-O(H)-Si bonds occurs at room temperature regardless of organic template protection, forming the rev-FAAl species (structures *D* and *E*), which adopt tetrahedral configurations as discussed above. In contrast, the Al-^{17}O-P signals ($\delta_1 \approx 70 \sim 90$ ppm) are absent in H-SAPO-34 (Fig. 3*C*) and AlPO-34 (*SI Appendix*, Fig. S10) after room-temperature $H_2{}^{17}O$ treatment, but are remarkable after steaming (*SI Appendix*, Fig. S11). In addition, despite the structural hydrolysis of DNL-6, SAPO-42, and SAPO-37 (Fig. 3*E* and *SI Appendix*, Fig. S12) after rehydration, the ^{17}O exchange of Al-O-P bonds is also extremely difficult at room temperature (*SI Appendix*, Fig. S13). This confirms that Al-O-P bonds exhibit good stability against hydrolysis at room temperature even in different topologies, which contradicts the conventional understanding of the hydrolytic characteristics of Al-O-P bonds. Therefore, both the rev-FAAl and irrev-FAAl species from $Al(OP)_4$ (structures *F* and *G*) are unambiguously excluded under hydration conditions.

It becomes apparent that intuitively associating the Al^{VI} signal with EFAl or FAAl is fallacious argument. Very distinct from aluminosilicate zeolites, the Al^{VI} species in SAPOs predominantly come from the FAl within $Al(OP)_4$ moiety that directly coordinates with two water molecules (as modeled in Fig. 2*I*), rather than from EFAl, FAAl, or FAl in $SiO(H)\text{-}Al(OP)_3$.

Degradation of SAPOs Under Ambient Atmospheres. Close attention has been paid to the degradation mechanism of SAPOs under ambient atmosphere. The prevalent view is that Al-O-P bonds are susceptible to hydrolysis, at least for the SAPOs with poor hydrothermal stability, based on the concomitant observation of large amounts of Al^{VI} and apparent loss of crystallinity in the XRD patterns after hydration. (39, 49, 54) Nevertheless, the dominant mechanism remains a subject of debate due to the complexity of the degradation process and the lack of atomic-scale understanding of defect species. This contribution provides a distinct viewpoint for the understanding of framework stability through the investigation of reversible hydrolysis via the ^{17}O tracing method. As mentioned above, Al-O-P bonds are stable against reversible hydrolysis at room temperature, even in the SAPOs with poor stability. Thus, the breakage of Al-O-P bonds is almost ruled out under neutral conditions, and the framework degradation is dominated by the irreversible hydrolysis of Al-O(H)-Si. This finding challenges the commonly accepted concept of SAPO stability, but it is rational and meaningful, as AlPOs generally exhibit superior hydrolysis stability relative to SAPOs.

Downloaded from https://www.pnas.org by CAS DALIAN INSTITUTE CHEMICAL PHYSICS on November 30, 2025 from IP address 119.78.131.208.

To further elucidate the degradation process, the structural details of hydroxyl group defects are required. The ^{1}H MAS NMR spectra in Fig. 3*E* show that all samples experience varying degrees of Brønsted acid site (BAS) degradation, accompanied by the formation of Al-OH defects at around 2.6 ppm. However, SAPO-34 exhibits good stability as evidenced by the substantial retention of BASs following 14 d of water immersion. The SAPOs with high Si contents are less stable since HSi-H-SAPO-34 (Fig. 3*E*) and HSi-H-DNL-6 (*SI Appendix*, Fig. S12) suffer more severe structural damage after water exposure due to the relatively poor stability of Al-O(H)-Si bonds. Notably, Si-OH signals are hardly present in these SAPOs, consistent with findings reported by Hunger in SAPO-34 and SAPO-37 (27). Despite the observation of Si-OH in HSi-SAPO-34 after redehydration, the quantity of this species almost equals the quantity before water exposure. This suggests that Si atoms are prone to completely dislodge from the framework and further aggregate with the consumption of silanol groups, which corresponds to the desilication mechanism. The ^{29}Si NMR spectra (*SI Appendix*, Fig. S14) also support the desilication mechanism, as the presence of broad signals at ca. -100 ppm suggests the formation of extraframework SiO_2 species in both steamed ^{29}Si-enriched H-SAPO-34 and room-temperature water-soaked H-DNL-6. Moreover, 2D ^{1}H TQ-SQ technique is utilized to investigate the three-spin proximity information, thereby providing insights into the fine atomic structures of defect species. As shown in Fig. 3*F*, the Al-OH species of steamed H-SAPO-34 at 2.4 ppm is self-correlated as a three-spin group, producing a TQ correlation at 7.2 ppm on the F1-axis, while the bridged hydroxyl groups at 3.4 to 3.8 ppm show no such proximity. This demonstrates the formation of Al-OH nests and concomitant tricoordinated framework Al (structures *I*, dehydration-derived products of structures *D*), which results from the framework desilication. Therefore, it is concluded that framework desilication is the dominant degradation mechanism of SAPOs after water exposure, resulting from the irreversible hydrolysis of Al-O(H)-Si rather than the hydrolysis of Al-O-P bonds.

Impacts of FAl Atoms on Water Adsorption. Building on the knowledge of Al^{VI} species, the coordination role of FAl in the host AlPO framework is expected to impact the adsorption behavior of polar guest molecules, which can decipher the adsorption nature of SAPOs and advance their applications. Fig. 4*A* compares the water adsorption isotherms of H-SAPO-34, H-SSZ-13, and AlPO-34 at 25 °C, showing that very steep rises occur for both H-SAPO-34 and AlPO-34 samples within a very narrow range of P/P_0 = 0.047~0.08. Even in arid environments (relative humidity, RH = 8%), H-SAPO-34 and AlPO-34 achieve 80% of the adsorption capacity measured in humid conditions (RH = 80%), whereas H-SSZ-13 shows significantly lower capacity. Moreover, the thermal analysis of water desorption (*SI Appendix*, Fig. S15 and Table S4) indicates that H-SAPO-34 has the highest total and average water desorption heat. Hence, the critical coordination role and high abundance of Al atoms in SAPOs enhance water adsorption and heat capacity. The detailed water adsorption behavior on BASs can be interpreted via the low-pressure adsorption stage, so the isotherms are replotted (Fig. 4*B*) on double logarithmic scales for zooming in on this region. During the stage of BAS adsorption, the isotherms can be subdivided into three steps according to the slope, with inflection points at 1, 2, and 6 water molecules per BAS (1.15, 2.3, 6.9 mmol/g) for H-SAPO-34, and 1, 2, and 4 per BAS (0.94, 1.9, 3.7 mmol/g) for H-SSZ-13. This suggests that the water molecules on BASs in both molecular sieves evolve from monomer to dimer and then to multimolecular adsorption. Furthermore, by controlling the dose and equilibrating for 2 d, ex-situ ^{27}Al spectra are recorded to examine the number of Al^{VI} in SAPO-34 with varying water adsorption amounts, as shown in Fig. 4*C*. Corresponding Al^{VI} contents and ^{31}P spectra are plotted in Fig. 4*D* and *SI Appendix*, Fig. S16, respectively. Three stages are distinguished based on the rate of formation of Al^{VI} species as a function of water loading. 1) Considering the water–proton complex $H(H_2O)_m$ or $H^+(H_2O)_m$, at loadings below 3.7 mmol/g H_2O (red region, corresponding to m = 1, 2, or 3), Al^{VI} species remains almost undetectable, as water primarily interacts with acidic protons. This demonstrates that the interaction between FAl and water is weaker not only than that between an isolated BAS and a single water molecule but also than that between a monomer ($H(H_2O)_1$) or dimer ($H(H_2O)_2$) and an additional water molecule. 2) At loadings of 3 to 6 water per BAS (orange region), minor Al^{VI} species gradually emerge, but the slope (Fig. 4*D*) is significantly lower than that at water loadings of over 6 per BAS (blue region). It is noteworthy that the stoichiometric number of 3 (i.e., m =3) corresponds well with the minimum water loading required for delocalization or solvation of Brønsted acids, as reported in previous theoretical calculations (55, 56). Moreover, the relative population of solvated proton is augmented with elevated water loading (57). This indicates that, while water–proton complexes remain the primary adsorption centers at this stage, the delocalization of protons means that trimers or larger complexes no longer exhibit significant energetic superiority in competitive adsorption against FAl. (3) At loadings exceeding 6 per BAS, since the interaction of the larger protonated clusters with additional water molecules is attenuated dramatically, the adsorption process is primarily driven by the FAl coordination, as indicated by very steep rises of the isotherm and the linear growth of Al^{VI} species with increasing water. Nevertheless, the quantity of adsorbed water is always more than twice that of Al^{VI}, as shown in *SI Appendix*, Fig. S17 (slope value ≈ 4, larger than 2), demonstrating the synergy of FAl coordination and capillary condensation (CC) via H-bonding interactions at this stage. Here, CC inherently occurs in nanoscale hydrophilic materials (58–60). It is the coordination effect of FAl (hydrophilicity enhancement) that promotes the CC process, since steep uptakes are observed only in SAPO-34 and AlPO-34, but not in H-SSZ-13. In addition, competitive adsorption between FAl and BASs is also reflected in the kinetic process, detailed in supporting information (*SI Appendix*, Fig. S18) via in situ ^{1}H and ^{27}Al NMR experiments.

In conclusion, Fig. 4*E* illustrates the evolution of adsorption centers in SAPOs with increasing water loading, which starts from the BAS center (including isolated BASs and water–proton complexes) to dual centers at both BASs and FAl within $Al(PO)_4$ framework, and eventually to primary FAl sites leading to CC that interlinks the water cluster within micropore confinement upon exceeding the P_c (the critical pressure at which steep uptakes begin, P_c/P_0 ≈ 0.047 for SAPO-34). BASs enhance the adsorption strength, while FAl atoms lead to a significant water uptake at a very low vapor pressure through CC. This establishes a foundation for predicting the onset of steep uptakes (P_c) for various dimensions of AlPOs/SAPOs according to the Kelvin equation. A larger pore opening would result in a higher P_c, and a rather small pore size increases P_c as well due to the steric hindrance. Furthermore, this insight advances the promising application of AlPO/SAPO materials in water adsorption fields, such as atmospheric water harvesting (AWH), refrigeration, seawater desalination, and air conditioning.

Conclusion. Detailed analysis of Al^{VI} species structures in SAPO molecular sieves reveals the host–guest interactions between SAPOs and water. Although the hydrolysis of SAPOs under

Downloaded from https://www.pnas.org by CAS DALIAN INSTITUTE CHEMICAL PHYSICS on November 30, 2025 from IP address 119.78.131.208.

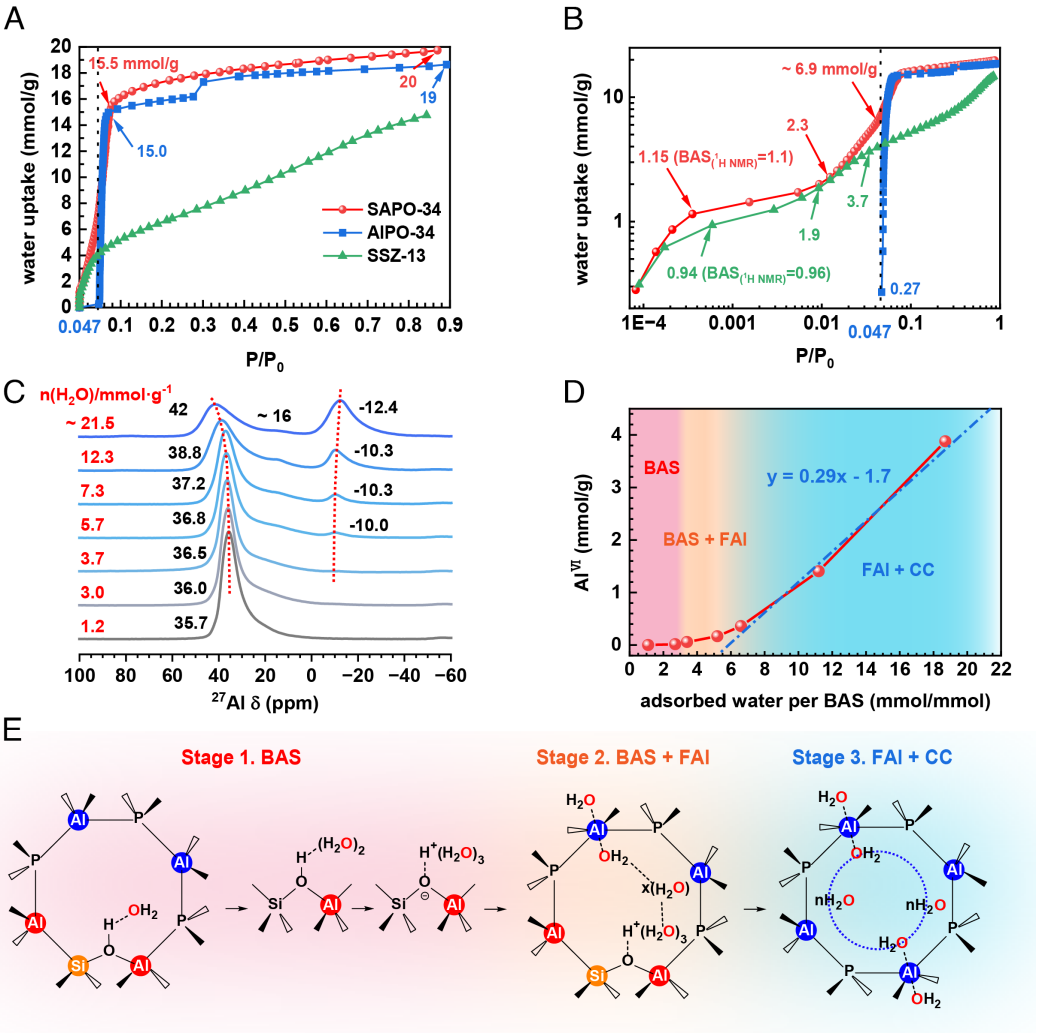

Fig. 4. Adsorption behavior of water in SAPO molecular sieve. (*A*) Water adsorption isotherms in H-SAPO-34, H-SSZ-13, and AlPO-34 at 25 °C, where the saturated vapor pressure (P_0) is 3.17 kPa. Dose feeding was performed instead of pressure control at the initial adsorption stage for the entire recording, as the isotherms included very steep uptakes at this stage. (*B*) Corresponding isotherms replotted on double logarithmic scales. (*C*) Ex-situ ^{27}Al MAS NMR spectra of H-SAPO-34 acquired at 11.7 T and corresponding Al^{VI} contents (*D*) with varying water loading. (*E*) Schematic of water molecules adsorption on H-SAPO-34. For simplicity, the adsorption structures of 2 and 3 molecules per BAS only depict the bridge hydroxyl group without showing the 8-member ring. At stage 2, the x value is from 1 to 3. The protonated structure of water trimer refers to the references. (55, 56)

hydration conditions widely occurs, associating the Al^{VI} species with the EFAl or FAAl, as is done in aluminosilicate zeolites, is highly misleading. Multiple complementary NMR methods were applied to sequentially rule out the primary contribution of EFAl, irrev-FAAl, and rev-FAAl to the Al^{VI} species. Additionally, despite the rapid and reversible hydrolysis in Al-O-Si and Al-OH-Si bonds, the Al species within these moieties are still tetrahedral. Therefore, our results modified the traditional understanding and confirmed that the Al^{VI} species predominantly adopt a FAl configuration within the $Al(OP)_4$ framework, coordinated to two water molecules (depicted in Fig. 2*I*). Furthermore, Al-O-P bonds possess better stability against hydrolysis than Al-O-Si and Al-OH-Si bonds under neutral conditions. Desilication, which forms Al-OH nests, potential tricoordinated framework Al, and aggregated extraframework Si atoms, has been identified as the dominant degradation mechanism of SAPOs under ambient conditions. Based on the structural knowledge of Al^{VI} species, the coordination of FAl atoms in the AlPO framework facilitates the adsorption of polar guest molecules and influences their adsorption behavior which is detailed with a combination of adsorption isotherm and ex-situ ^{27}Al NMR spectra. Moreover, in situ kinetic ^{1}H and ^{27}Al NMR experiments reveal the competitive adsorption between FAl and BASs during the initial adsorption phase and elucidate the adsorption kinetics.

From application perspectives, this work has validated the weak acidity (coordinations and moderate hydrophilicity) and high stability of the AlPO host framework against hydrolysis, establishing a theoretical foundation for the promising applications of SAPOs/AlPOs in water adsorption technologies such as refrigeration, AWH, seawater desalination, and air conditioning. Moreover, it opens up opportunities for reusing deactivated catalysts that have partially lost their BASs in water adsorption fields. Additionally, the study offers crucial insights into adjusting adsorption strength and critical pressure by optimizing the number and type of isomorphous heteroatoms (such as Si atom for SAPO, and Zn for ZAPO) and pore opening, thereby improving adsorption performance.

Materials and Methods

Materials and Characterization. Zeolites were all synthesized by traditional hydrothermal methods with organic structure-directing agents. All samples were freshly calcined at 550 to 600 °C for 4 to 6 h to remove the template or NH_3 before characterization and posttreatment. Detailed synthetic information and characterization of materials are provided in *SI Appendix*.

Downloaded from https://www.pnas.org by CAS DALIAN INSTITUTE CHEMICAL PHYSICS on November 30, 2025 from IP address 119.78.131.208.

General Methods. A comprehensive suite of solid-state NMR techniques was employed to identify the Al species. NMR experiments were conducted on Bruker Avance NEO 500 MHz (11.7 T wide-bore magnet) and Bruker Avance III 600 MHz (14.1 T wide-bore magnet) spectrometers using 3.2 mm HX MAS, 3.2 mm HXY triple resonance MAS, 4 mm HX MAS, and 4 mm WVT MAS probes. As detailed in *SI Appendix*, the typical radiofrequency (RF) field strengths of ^{1}H, ^{27}Al, ^{29}Si, and ^{31}P were 96, 58, 68, and 86 kHz, respectively. 2D NMR spectroscopy was applied to determine the framework structures. Chemical shifts were referenced to adamantane (^{1}H, 1.74 ppm), H_2O (^{17}O, 0 ppm), 1 M $Al(NO_3)_3$ (^{27}Al, 0 ppm), kaolinite (^{29}Si, -91.5 ppm), and $NH_4H_2PO_4$ (^{31}P, 1.0 ppm), respectively. The water adsorption isotherms were collected on a 3Flex adsorption analyzer from Micromeritics Instrument Corporation. The water desorption enthalpy of samples was assessed by a thermogravimetric analyzer (TG-DSC, STA449F5, NETZSCH Co., Germany). Dehydrated zeolites were prepared in the vacuum line ($< 10^{-3}$ Pa) via a stepwise procedure to a final temperature of 693 K throughout 12 h, and then packed into ZrO_2 rotors under an Ar atmosphere. Hydrated samples were obtained by adding the determined volume of H_2O into the rotors of dehydrated samples, typically by adding 10 μL H_2O into the rotors containing about 20 mg of dehydrated samples and allowing them to equilibrate overnight. The redehydrated samples were prepared by dehydrating the hydrated samples within the rotor via the vacuum line at desired temperatures overnight. ^{17}O trace experiments were performed on all samples following vacuum dehydration to avoid ^{17}O isotopic dilution by adsorbed water. Room-temperature-treated samples were prepared by mixing the dehydrated samples with 90% ^{17}O-labeled H_2O, using a ratio of approximately 50 mg of catalyst to 20 μL of $H_2{}^{17}O$, in 4 mm ZrO_2 rotors, with the mixture being allowed to react for 2 to 7 d. Samples subjected to high-temperature steam treatment were processed in autoclaves using a tuft of quartz wool to separate the solid zeolite from liquid water. All samples intended for ^{17}O NMR analysis were vacuum-dehydrated after water treatment to eliminate the adsorbed $H_2{}^{17}O$. DFT calculations were carried out for geometry optimization and transition state location using the Vienna Ab initio Simulation Package with the PBE exchange-correlation functional. All associated experimental data and comprehensive computational protocols are provided in *SI Appendix*.

Data, Materials, and Software Availability. All study data are included in the article and/or *SI Appendix*.

ACKNOWLEDGMENTS. We would like to thank Prof. Jean-Paul Amoureux (Univ. Lille, France) and Dr. Akiko Sasaki (Bruker Japan K. K, Japan) for their valuable assistance in the implementation of soft-pulse-added-mixing approach. This work was supported by the National Natural Science Foundation of China (22288101; 22241801; 22022202; 22032005; 21991090; 21991092; 21991093; 22072148; 22372164; and 22372169); National Key Research and Development Program of China (No. 2022YFE0116000); Dalian Outstanding Young Scientist Foundation (2021RJ01); Natural Science Foundation of Liaoning Province of China (2022-MS-029); and Liaoning International Joint Laboratory Project (2024JH2/102100005).

Author affiliations: [a]National Engineering Research Center of Lower-Carbon Catalysis Technology, Dalian Institute of Chemical Physics, Chinese Academy of Sciences, Dalian 116023, China; [b]University of Chinese Academy of Sciences, Beijing 100049, China; [c]State Key Laboratory of Catalysis, Dalian Institute of Chemical Physics, Chinese Academy of Sciences, Dalian 116023, China; and [d]State Key Laboratory of Inorganic Synthesis and Preparative Chemistry, College of Chemistry, Jilin University, Changchun 130012, China

1. X. F. Yi *et al.*, Adsorbate-driven dynamic active sites in stannosilicate zeolites. *Fundam. Res.* **5**, 174–182 (2025). 10.1016/j.fmre.2022.12.015.
2. B. Y. Shen *et al.*, Atomic imaging of zeolite-confined single molecules by electron microscopy. *Nature* **607**, 703–707 (2022). 10.1038/s41586-022-04876-x.
3. H. Xiong *et al.*, In situ imaging of the sorption-induced subcell topological flexibility of a rigid zeolite framework. *Science* **376**, 491–496 (2022). 10.1126/science.abn7667.
4. B. Y. Shen *et al.*, A single-molecule van der Waals compass. *Nature* **592**, 541–544 (2021). 10.1038/s41586-021-03429-y.
5. B. T. W. Lo *et al.*, Elucidation of adsorbate structures and interactions on Brønsted acid sites in H-ZSM-5 by synchrotron X-ray powder diffraction. *Angew. Chem. Int. Ed.* **55**, 5981–5984 (2016). 10.1002/anie.201600487.
6. Q. Liu, J. A. van Bokhoven, Water structures on acidic zeolites and their roles in catalysis. *Chem. Soc. Rev.* **53**, 3065–3095 (2024). 10.1039/d3cs00404j.
7. Z. P. Hu, J. F. Han, Y. X. Wei, Z. M. Liu, Dynamic evolution of zeolite framework and metal-zeolite interface. *ACS Catal.* **12**, 5060–5076 (2022). 10.1021/acscatal.2c01233.
8. D. E. Resasco, S. P. Crossley, B. Wang, J. L. White, Interaction of water with zeolites: A review. *Catal. Rev.* **63**, 302–362 (2021). 10.1080/01614940.2021.1948301.
9. K. Stanciakova, B. M. Weckhuysen, Water-active site interactions in zeolites and their relevance in catalysis. *Trends Chem.* **3**, 456–468 (2021). 10.1016/j.trechm.2021.03.004.
10. D. T. Bregante *et al.*, The shape of water in zeolites and its impact on epoxidation catalysis. *Nat. Catal.* **4**, 797–808 (2021). 10.1038/s41929-021-00672-4.
11. S. Eckstein *et al.*, Influence of hydronium ions in zeolites on sorption. *Angew. Chem. Int. Ed.* **58**, 3450–3455 (2019). 10.1002/anie.201812184.
12. L. Smith *et al.*, On the nature of water bound to a solid acid catalyst. *Science* **271**, 799–802 (1996). 10.1126/science.271.5250.799.
13. Z. L. Liu *et al.*, Ultralow-temperature-driven water-based sorption refrigeration enabled by low-cost zeolite-like porous aluminophosphate. *Nat. Commun.* **13**, 193 (2022). 10.1038/s41467-021-27883-4.
14. S. T. Xu *et al.*, Advances in catalysis for methanol-to-olefins conversion. *Adv. Catal.* **61**, 37–122 (2017). 10.1016/bs.acat.2017.10.002.
15. K. C. Khulbe, T. Matsuura, C. Y. Feng, A. F. Ismail, Recent development on the effect of water/moisture on the performance of zeolite membrane and MMMs containing zeolite for gas separation; Review. *RSC Adv.* **6**, 42943–42961 (2016). 10.1039/c6ra03007f.
16. P. Tian, Y. X. Wei, M. Ye, Z. M. Liu, Methanol to olefins (MTO): From fundamentals to commercialization. *ACS Catal.* **5**, 1922–1938 (2015). 10.1021/acscatal.5b00007.
17. C. Y. Nie *et al.*, Unraveling a stable 16-ring aluminophosphate DNL-11 through three-dimensional electron diffraction for atmospheric water harvesting. *J. Am. Chem. Soc.* **146**, 10257–10262 (2024). 10.1021/jacs.4c01393.
18. T. Kohler, M. Hinze, K. Müller, W. Schwieger, Temperature independent description of water adsorption on zeotypes showing a type V adsorption isotherm. *Energy* **135**, 227–236 (2017). 10.1016/j.energy.2017.06.115.
19. U. Lohse, M. Noack, E. Jahn, Adsorption properties of the $AlPO_4$-5 molecular sieve. *Adsorpt. Sci. Technol.* **3**, 19–24 (1986). 10.1177/026361748600300104.
20. G. C. Li *et al.*, Thermal alteration in adsorption sites over SAPO-34 zeolite. *Angew. Chem. Int. Ed.* **61**, e202204500 (2022). 10.1002/anie.202204500.
21. G. C. Li *et al.*, Induced active sites by adsorbate in zeotype materials. *J. Am. Chem. Soc.* **143**, 8761–8771 (2021). 10.1021/jacs.1c03166.
22. Z. B. Li, J. Martinez-Triguero, P. Concepcion, J. H. Yu, A. Corma, Methanol to olefins: Activity and stability of nanosized SAPO-34 molecular sieves and control of selectivity by silicon distribution. *Phys. Chem. Chem. Phys.* **15**, 14670–14680 (2013). 10.1039/c3cp52247d.
23. J. Bauer *et al.*, Stability of AlPO and SAPO molecular sieves during adsorption-desorption cycles of water vapor investigated by in-situ XRD measurements. *Stud. Surf. Sci. Catal.* **170**, 837–844 (2007). 10.1016/S0167-2991(07)80930-X.
24. X. W. Wang, J. Coleman, X. Jia, J. L. White, Quantitative investigations of acidity, and transient acidity, in zeolites and molecular sieves. *J. Phys. Chem. B* **106**, 4941–4946 (2002). 10.1021/jp0145816.
25. B. Parlitz, U. Lohse, E. Schreier, Hydrolysis of -P-O-Al bonds in $AlPO_4$ and SAPO molecular sieves. *Microporous Mater.* **2**, 223–228 (1994). 10.1016/0927-6513(93)e0054-k.
26. M. Briend, A. Shikholeslami, M. J. Peltre, D. Delafosse, D. Barthomeuf, Thermal and hydrothermal stability of SAPO-5 and SAPO-37 molecular sieves. *J. Chem. Soc. Dalton Trans.* **7**, 1361–1362 (1989). 10.1039/dt9890001361.
27. A. Buchholz, W. Wang, A. Arnold, M. Xu, M. Hunger, Successive steps of hydration and dehydration of silicoaluminophosphates H-SAPO-34 and H-SAPO-37 investigated by in situ CF MAS NMR spectroscopy. *Microporous Mesoporous Mater.* **57**, 157–168 (2003). 10.1016/S1387-1811(02)00562-0.
28. C. J. Heard *et al.*, Fast room temperature lability of aluminosilicate zeolites. *Nat. Commun.* **10**, 4690 (2019). 10.1038/s41467-019-12752-y.
29. S. M. Pugh, P. A. Wright, D. J. Law, N. Thompson, S. E. Ashbrook, Facile, room-temperature ^{17}O enrichment of zeolite frameworks revealed by solid-state NMR spectroscopy. *J. Am. Chem. Soc.* **142**, 900–906 (2020). 10.1021/jacs.9b10528.
30. T. T. Sun *et al.*, Water-induced structural dynamic process in molecular sieves under mild hydrothermal conditions: Ship-in-a-bottle strategy for acidity identification and catalyst modification. *Angew. Chem. Int. Ed.* **59**, 20672–20681 (2020). 10.1002/anie.202009648.
31. L. Yang *et al.*, Stabilizing the framework of SAPO-34 zeolite toward long-term methanol-to-olefins conversion. *Nat. Commun.* **12**, 4661 (2021). 10.1038/s41467-021-24403-2.
32. Y. Watanabe, A. Koiwai, H. Takeuchi, S. A. Hyodo, S. Noda, Multinuclear NMR studies on the thermal stability of SAPO-34. *J. Catal.* **143**, 430–436 (1993). 10.1006/jcat.1993.1287.
33. M. Afeworki, G. Cao, D. L. Dorset, K. G. Strohmaier, G. J. Kennedy, Multinuclear and multidimensional solid-state NMR characterization of EMM-8. *Microporous Mesoporous Mater.* **103**, 216–224 (2007). 10.1016/j.micromeso.2007.01.048.
34. S. Al-Nahari *et al.*, Impact of mineralizing agents on aluminum distribution and acidity of ZSM-5 zeolites. *Angew. Chem. Int. Ed.* **62**, e202217992 (2022). 10.1002/anie.202217992.
35. K. Z. Chen, Z. H. Gan, S. Horstmeier, J. L. White, Distribution of aluminum species in zeolite catalysts: ^{27}Al NMR of framework, partially-coordinated framework, and non-framework moieties. *J. Am. Chem. Soc.* **143**, 6669–6680 (2021). 10.1021/jacs.1c02361.
36. M. Ravi, V. L. Sushkevich, J. A. van Bokhoven, Towards a better understanding of Lewis acidic aluminium in zeolites. *Nat. Mater.* **19**, 1047–1056 (2020). 10.1038/s41563-020-0751-3.
37. Z. W. Yu *et al.*, Insights into the dealumination of zeolite HY revealed by sensitivity-enhanced ^{27}Al DQ-MAS NMR spectroscopy at high field. *Angew. Chem. Int. Ed.* **49**, 8657–8661 (2010). 10.1002/anie.201004007.
38. G. Agostini *et al.*, In situ XAS and XRPD parametric rietveld refinement to understand dealumination of Y zeolite catalyst. *J. Am. Chem. Soc.* **132**, 667–678 (2010). 10.1021/ja907696h.
39. J. A. van Bokhoven, D. C. Koningsberger, P. Kunkeler, H. van Bekkum, A. P. M. Kentgens, Stepwise dealumination of zeolite beta at specific T-sites observed with ^{27}Al MAS and ^{27}Al MQ MAS NMR. *J. Am. Chem. Soc.* **122**, 12842–12847 (2000). 10.1021/ja002689d.
40. M. Haouas, A. Kogelbauer, R. Prins, The effect of flexible lattice aluminium in zeolite beta during the nitration of toluene with nitric acid and acetic anhydride. *Catal. Lett.* **70**, 61–65 (2000). 10.1023/A:1019015216483.

Downloaded from https://www.pnas.org by CAS DALIAN INSTITUTE CHEMICAL PHYSICS on November 30, 2025 from IP address 119.78.131.208.

41. B. H. Wouters, T. H. Chen, P. J. Grobet, Reversible tetrahedral-octahedral framework aluminum transformation in zeolite Y. *J. Am. Chem. Soc.* **120**, 11419–11425 (1998). 10.1021/ja982082l.
42. J. Brus *et al.*, Structure of framework aluminum Lewis sites and perturbed aluminum atoms in zeolites as determined by ^{27}Al{^{1}H} REDOR (3Q) MAS NMR spectroscopy and DFT/molecular mechanics. *Angew. Chem. Int. Ed.* **54**, 541–545 (2015). 10.1002/anie.201409635.
43. A. P. M. Kentgens, D. Iuga, M. Kalwei, H. Koller, Direct observation of Bronsted acidic sites in dehydrated zeolite H-ZSM5 using DFS-enhanced ^{27}Al MQMAS NMR spectroscopy. *J. Am. Chem. Soc.* **123**, 2925–2926 (2001). 10.1021/ja005917c.
44. C. P. Grey, A. J. Vega, Determination of the quadrupole coupling constant of the invisible aluminum spins in zeolite HY with ^{1}H/^{27}Al TRAPDOR NMR. *J. Am. Chem. Soc.* **117**, 8232–8242 (1995). 10.1021/Ja00136a022.
45. S. H. Xin *et al.*, The acidic nature of "NMR-invisible" tri-coordinated framework aluminum species in zeolites. *Chem. Sci.* **10**, 10159–10169 (2019). 10.1039/c9sc02634g.
46. X. F. Yi *et al.*, Origin and structural characteristics of tri-coordinated extra-framework aluminum species in dealuminated zeolites. *J. Am. Chem. Soc.* **140**, 10764–10774 (2018). 10.1021/jacs.8b04819.
47. Y. Ji, K. Z. Chen, X. W. Han, X. H. Bao, G. J. Hou, Precise structural and dynamical details in zeolites revealed by coupling-edited ^{1}H–^{17}O double resonance NMR spectroscopy. *J. Am. Chem. Soc.* **146**, 11211–11224 (2024). 10.1021/jacs.3c14787.
48. L. Smith *et al.*, A quantitative description of the active sites in the dehydrated acid catalyst HSAPO-34 for the conversion of methanol to olefins. *Catal. Lett.* **41**, 13–16 (1996). 10.1007/Bf00811705.
49. H. L. Zubowa *et al.*, Synthesis and properties of the silicoaluminophosphate molecular sieve SAPO-31. *J. Chem. Soc. Faraday Trans.* **86**, 2307–2312 (1990). 10.1039/ft9908602307.
50. Z. H. Gan, H. T. Kwak, Enhancing MQMAS sensitivity using signals from multiple coherence transfer pathways. *J. Magn. Reson.* **168**, 346–351 (2004). 10.1016/j.jmr.2004.03.021.
51. A. Sasaki, Y. Tsutsumi, J. P. Amoureux, Accelerating high-resolution NMR of half-integer quadrupolar nuclei in solids: SPAM-MQMAS and SPAM-STMAS. *Solid State Nucl. Magn. Reson.* **108**, 101668 (2020). 10.1016/j.ssnmr.2020.101668.
52. J. P. Amoureux *et al.*, Implementing SPAM into STMAS: A net sensitivity improvement in high-resolution NMR of quadrupolar nuclei. *J. Magn. Reson.* **175**, 285–299 (2005). 10.1016/j.jmr.2005.05.002.
53. J. P. Amoureux *et al.*, Increasing the sensitivity of 2D high-resolution NMR methods applied to quadrupolar nuclei. *J. Magn. Reson.* **172**, 268–278 (2005). 10.1016/j.jmr.2004.11.001.
54. G. N. Kalantzopoulos *et al.*, Factors determining microporous material stability in water: The curious case of SAPO-37. *Chem. Mater.* **32**, 1495–1505 (2020). 10.1021/acs.chemmater.9b04510.
55. E. Grifoni *et al.*, Confinement effects and acid strength in zeolites. *Nat. Commun.* **12**, 2630 (2021). 10.1038/s41467-021-22936-0.
56. V. Termath, F. Haase, J. Sauer, J. Hutter, M. Parrinello, Understanding the nature of water bound to solid acid surfaces. Ab initio simulation on HSAPO-34. *J. Am. Chem. Soc.* **120**, 8512–8516 (1998). 10.1021/ja981549p.
57. M. Wang *et al.*, Genesis and stability of hydronium ions in zeolite channels. *J. Am. Chem. Soc.* **141**, 3444–3455 (2019). 10.1021/jacs.8b07969.
58. Q. Yang *et al.*, Capillary condensation under atomic-scale confinement. *Nature* **588**, 250–253 (2020). 10.1038/s41586-020-2978-1.
59. N. Mameka, J. Markmann, J. Weissmüller, On the impact of capillarity for strength at the nanoscale. *Nat. Commun.* **8**, 1976 (2017). 10.1038/s41467-017-01434-2.
60. J. W. van Honschoten, N. Brunets, N. R. Tas, Capillarity at the nanoscale. *Chem. Soc. Rev.* **39**, 1096–1114 (2010). 10.1039/b909101g.

Downloaded from https://www.pnas.org by CAS DALIAN INSTITUTE CHEMICAL PHYSICS on November 30, 2025 from IP address 119.78.131.208.